World Journal of Advanced Engineering Technology and Sciences
eISSN: 2582-8266
Cross Ref DOI: 10.30574/wjaets
Journal homepage: https://wjaets.com/

(RESEARCH ARTICLE)

Check for updates

OPTIMIZATION OF ROOM-TEMPERATURE SPIN INJECTION IN COMMERCIAL VCSELS USING AN EXTENDED SPIN-FLIP MODEL

Yevgeniy Muralev *

Department of Energy, Engineering Faculty, Yessenov University, Aktau, Kazakhstan.
* Corresponding Author

ORCID Details
Yevgeniy Muralev: https://orcid.org/0009-0006-6041-6341

World Journal of Advanced Engineering Technology and Sciences, 2026, 21(02), 192–201

Publication history: Received on 01 October 2026; revised on 08 November 2026; accepted on 10 November 2026

Article DOI: https://doi.org/10.30574/wjaets.2026.21.2.0498

Copyright © 2026 Author(s) retain the copyright of this article. This article is published under the terms of the Creative Commons Attribution License 4.0

ABSTRACT

Spin lasers exploit the quantum mechanical coupling between electron spin orientation and photon polarization, offering compelling advantages in threshold reduction, modulation bandwidth, and all-optical data processing. Despite considerable theoretical progress, the practical demonstration of spin injection into commercially available devices at room temperature under non-resonant excitation wavelengths remains limited. Here, we report the successful room-temperature spin injection into a commercial 845 nm vertical cavity surface emitting laser (VCSEL) using pulsed optical pumping at two wavelengths corresponding to non-resonant cavity dips: 794 nm (dip A) and 810 nm (dip B). We achieved a maximum degree of circular polarization (DCP) of approximately 20% at 794 nm excitation and approximately 5% at 810 nm. The wavelength dependence was interpreted through the optical selection rules governing transitions in bulk GaAs at finite crystal momentum ($k \neq 0$): excitation further from the band edge enhances the heavy-hole contribution relative to the light-hole band, thereby increasing the net spin polarization. To provide a quantitative framework, we extended the well-established spin-flip model (SFM) by introducing a wavelength-dependent pump polarization parameter P, which captures the effective spin injection efficiency under realistic optical pumping conditions without increasing the number of experimentally inaccessible free parameters. The extended SFM reproduces the measured polarization trends at both wavelengths in excellent agreement with the experiment. These findings establish a practical roadmap for optimizing spin injection in commercial VCSEL platforms and underline their potential as accessible building blocks for all-optical logic, neuromorphic photonics, and spin-based radio-over-fiber systems.

Keywords: Spin VCSEL; Spin-Flip Model; Optical Spin Injection; Circular Polarisation; GaAs Selection Rules; Spintronics; Photonics

1 INTRODUCTION

The fundamental quantum mechanical relationship between electron spin orientation and emitted photon polarization is the operating principle of spin lasers—semiconductor gain devices in which the carrier spin degree of freedom provides a controllable internal degree of freedom that is absent in conventional lasers [1]. Spin lasers have attracted sustained research interest because they offer several performance advantages over their spin-unpolarized

counterparts. Chief among these is a reduction in the threshold current: when spin-polarized carriers are injected, the population inversion required for lasing can be reached with fewer total carriers, lowering the drive power and improving energy efficiency [1]. Beyond threshold behavior, spin lasers support substantially faster amplitude and polarization modulation than conventional devices because the spin dynamics introduce an additional oscillation frequency that lies well above the classical relaxation-oscillation frequency [3, 27]. This modulation advantage has been exploited in proof-of-concept demonstrations of spin-VCSEL transmitters for analog radio-over-fiber links targeted at 5G and beyond [5]. At a more exploratory level, the controllable polarization state of the spin laser output is a natural resource for all-optical processing, enabling time-delayed reservoir computing, neuromorphic photonic circuits, and reconfigurable Boolean logic entirely within the optical domain [6–8].

The practical implementation of spin lasers calls for a device architecture that simultaneously provides strong spin–photon coupling, compatibility with room-temperature operation, and compatibility with existing photonic integration platforms. Vertical cavity surface emitting lasers (VCSELs) satisfy all three requirements. VCSELs are manufactured in large volumes, are fully compatible with standard fiber-optic interconnect infrastructure, and their circular aperture geometry naturally supports circularly polarized modes, making them the preferred host platform for spin injection experiments [12, 13]. Spin injection into VCSEL structures has been achieved by electrical injection through ferromagnetic contacts, by resonant optical pumping, and by non-resonant optical pumping using circularly polarized light tuned to an absorbing cavity resonance distinct from the laser mode [14–16]. Non-resonant optical pumping is particularly attractive for benchmarking purposes because it decouples the spin injection process from the lasing dynamics, allowing independent control of the injected spin polarization and the threshold behavior of the device.

Despite this progress, a recurring limitation of non-resonant optical spin injection into commercial VCSELs is that the available pump wavelengths are dictated by the VCSEL's reflectivity spectrum rather than by the experimenter's choice. In a standard 850 nm VCSEL, the high-reflectivity stopband typically spans roughly 820–870 nm, and only the narrow transmission dips on the short-wavelength shoulder of the stopband provide viable entry points for optical spin pumping. These dips lie at energies that may be tens to hundreds of meV above the GaAs band edge, placing the excitation at finite crystal momentum where the optical selection rules differ substantially from the simple Γ-point picture [19]. This wavelength dependence of spin injection efficiency has been characterized in GaAs quantum-well systems [11] but has not previously been quantitatively modelled for the specific case of commercial VCSEL optical pumping at non-ideal wavelengths.

The spin-flip model (SFM) originally developed by San Miguel, Feng, and Moloney and extended algebraically by Adams and co-workers provides a compact and experimentally tractable framework for describing the polarization dynamics of VCSELs under spin-polarized pumping [2, 17]. However, the standard SFM formulation assumes a fixed pump polarization degree P, which is an independent input parameter and does not account for the wavelength dependence of P arising from the semiconductor selection rules and band structure at $k \neq 0$. In this study, we close this gap. We present room-temperature spin injection experiments on a commercial 845 nm VCSEL at two non-resonant pump wavelengths (794 nm and 810 nm), observe a factor-of-four difference in maximum DCP (degree of circular polarization) between the two wavelengths, and develop an extended SFM formulation in which the pump polarization P is treated as a wavelength-dependent fitting parameter encoding the effective spin injection efficiency. The extended model reproduces the experimental power-dependent and asymptotic polarization trends at both wavelengths, providing a predictive framework for optimizing spin injection in commercial VCSEL platforms.

2 METHODS

2.1 Device and Packaging

Experiments were performed on a commercially sourced 845 nm single-mode VCSEL (HFE4192-581, 4.25 Gbps) packaged in a TO-46 header [18]. To enable direct optical access to the epitaxial surface, the plastic collimating lens and protective casing were mechanically removed. The bare VCSEL die was mounted on a custom temperature-controlled stage incorporating a thermoelectric (Peltier) element and a calibrated thermistor, driven by a Thorlabs TCC001 thermocontroller. This arrangement maintained the device temperature to better than 0.1 °C throughout data acquisition, eliminating thermal drift of the lasing wavelength and threshold current. Electrical pumping was supplied by a Thorlabs KLD101 low-noise current source.

2.2 Optical Pumping and Collection

Optical spin pumping was performed using circularly polarized pulses of duration 2.4 ps generated by a tunable diode-pumped Ti:Sapphire laser (Spectra Physics Tsunami). Two center wavelengths were selected to coincide with the absorption dips in the VCSEL reflectivity spectrum: approximately 793–794 nm (dip A) and 810 nm (dip B). The pump beam was focused onto the VCSEL output facet through an achromatic microscope objective, as shown in Figure 1a (focal length 7.5 mm). Polarization was controlled using a combination of half-wave and quarter-wave plates arranged

to produce either σ^+ or σ^- circularly polarized excitation. The VCSEL emission was collected in reflection geometry by the same objective, separated from the pump by a beam splitter, and directed through an independent waveplate analyzer set to resolve the σ^+ and σ^- components of the emission. Spectra were dispersed by a Princeton Instruments TriVista triple spectrometer and recorded using a liquid-nitrogen-cooled CCD camera.

2.3 Reflectivity Characterization

The VCSEL reflectivity was measured using a fiber-coupled broadband white-light source and normalized against the response of a calibrated silver mirror. The normalized spectrum shown in Figure 1b allows unambiguous identification of the distributed Bragg reflector (DBR) stopband and the transmission dips that serve as optical injection ports. The central stopband spans approximately 820–870 nm; the laser mode appears as a narrow shallow dip near 845 nm at the stopband center. Two pronounced transmission dips on the short-wavelength shoulder, labelled A (≈ 793 nm) and B (≈ 810 nm), were identified as viable optical pumping windows.

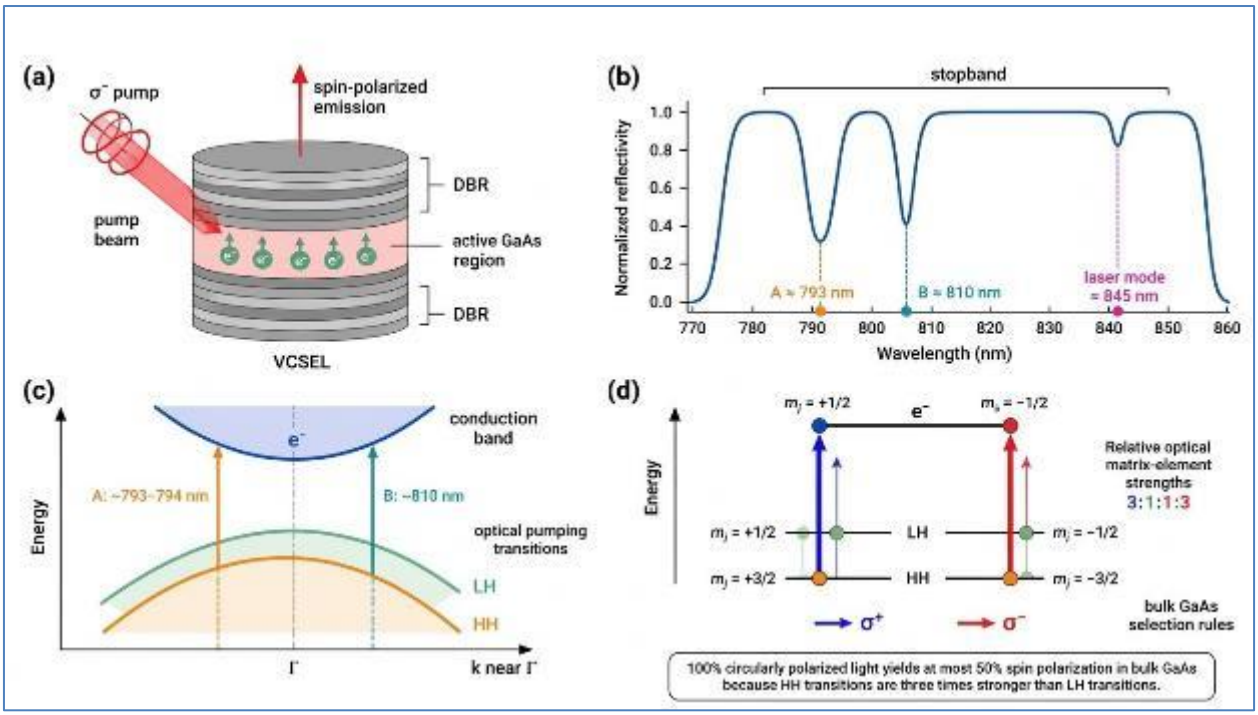


Figure 1: Optical spin pumping and selection rules in a VCSEL. (a) Schematic of circularly polarised optical pumping and spin-polarised emission from a VCSEL. (b) Normalised reflectivity spectrum showing the DBR stopband, pump windows A and B, and the laser mode. (c) Schematic GaAs band structure and optical pumping transitions near the Γ point. (d) Bulk-GaAs selection rules and relative heavy-hole and light-hole transition strengths.

2.4 Degree of Circular Polarisation

The degree of circular polarization (DCP), or third Stokes parameter S_3, was calculated from the integrated σ^+ and σ^- spectral intensities according to equation (1):

$$S_3 = \frac{I^+ - I^-}{I^+ + I^-} \qquad (1)$$

In equation (1), I^+ (I^-) is the spectrally integrated intensity of the σ^+ (σ^-) emission component. The parameter S_3 ranges from −1 (fully left-circularly polarized) to +1 (fully right-circularly polarized), with zero indicating no net circular polarization.

2.5 Extended Spin-Flip Model

The spin-flip model (SFM) used here follows the algebraic formulation of Adams et al. [17], based on the rate equations originally proposed by San Miguel, Feng, and Moloney. The VCSEL field is decomposed into right- and left-circularly polarized components with slowly varying real amplitudes R_+ and R_-. The normalized carrier variables N and m are proportional to the sum ($n^+ + n^-$) and difference ($n^+ - n^-$), respectively, of the spin-resolved carrier concentrations. The model parameters, with the carrier-field coupling shown schematically in Figure 4a, are the photon-field decay rate κ,

carrier recombination rate γ, effective spin-relaxation rate γ_s, birefringence γ_p, dichroism γ_a, and linewidth-enhancement factor α. The complete dynamical system is given by Equations (2)–(6):

$$\frac{dR_+}{dt} = \kappa(N + m - 1)R_+ - \left(\tilde{\gamma}_a \cos\phi + \gamma_p^+ \sin\phi\right)R_- \quad (2)$$

$$\frac{dR_-}{dt} = \kappa(N - m - 1)R_- - \left(\tilde{\gamma}_a \cos\phi - \gamma_p^- \sin\phi\right)R_+ \quad (3)$$

$$\frac{d\phi}{dt} = 2\kappa\alpha m + \tilde{\gamma}_a \sin\phi \left(\frac{R_+}{R_-} + \frac{R_-}{R_+}\right) + \cos\phi \left(\gamma_p^+ \frac{R_-}{R_+} - \gamma_p^- \frac{R_+}{R_-}\right) \quad (4)$$

$$\frac{dN}{dt} = \gamma[\eta - (1 + R_+^2 + R_-^2)N - (R_+^2 - R_-^2)m] \quad (5)$$

$$\frac{dm}{dt} = \gamma P\eta - [\gamma_s + \gamma(R_+^2 + R_-^2)]m - \gamma(R_+^2 - R_-^2)N \quad (6)$$

In Equations (2)–(6), $\gamma_p^+ = \gamma_p - \gamma_a \sin(2\theta)$, $\gamma_p^- = \gamma_p + \gamma_a \sin(2\theta)$, and $\bar{\gamma}_a = \gamma_a \cos(2\theta)$; φ is the phase difference between R_+ and R_-, and θ is the angle between the principal birefringence and dichroism axes [17].

When the carrier recombination time is much longer than both the spin-relaxation time and the photon lifetime, that is, $\gamma \ll \gamma_s$ and $\gamma \ll \kappa$, equations (2)–(6) admit a closed-form steady-state reduction [17]. For aligned birefringence and dichroism axes (θ = 0), as assumed in the present calculations, the pump polarization and output ellipticity are related by equation (7):

$$P = \frac{\varepsilon}{\eta}\left\{\eta - 1 \pm \frac{\gamma_s(\gamma_a^2 + \gamma_p^2)}{\gamma\kappa\sqrt{1-\varepsilon^2}\sqrt{(\gamma_a + \alpha\gamma_p)^2 + \varepsilon^2(\alpha\gamma_a - \gamma_p)^2}}\right\} \quad (7)$$

In equation (7), $\varepsilon = (R_+^2 - R_-^2)/(R_+^2 + R_-^2)$ is the emission ellipticity, η is the normalized pump rate, and $P = (\eta_+ - \eta_-)/(\eta_+ + \eta_-)$ is the pump polarization degree. The ± sign represents the two steady-state phase branches of the SFM. For direct comparison with the measured pump power, η is defined by equation (8):

$$\eta = \frac{P_p}{P_{\text{th}}} \quad (8)$$

In equation (8), P_p is the incident optical pump power and P_{th} = 7 mW is the measured lasing threshold power. Thus, η = 1 at the threshold, consistent with the normalization used in Figure 4. The parameters used for all calculations are listed in Table 1.

Table 1: Spin-flip model parameters used in this work.

Parameter	Definition	Value	Reference
γ	Carrier recombination rate	1 ns^{-1}	[17]
γ_s	Spin relaxation rate	50 ns^{-1}	[4]
γ_a	Dichroism	0.2 ns^{-1}	[17]
γ_p	Birefringence	10 ns^{-1}	[17]
α	Linewidth enhancement factor	2	[22]
κ	Photon field decay rate	125 ns^{-1}	[23]

Extension to wavelength-dependent injection. In the standard SFM, P is a fixed independent parameter. In our extension, P is treated as a wavelength-dependent effective pump polarization that encodes the selection-rule-weighted spin injection efficiency at each excitation wavelength. Rather than introducing additional parameters to model the excited-state relaxation from the pump wavelength to the lasing state—which would add experimentally inaccessible free parameters to an already heavily parameterized model—we fit P independently for the two pump wavelengths and interpret the resulting values in terms of the known selection rules of GaAs at finite k. All intrinsic VCSEL parameters (κ, γ, γ_s, γ_p, γ_a, α) remain fixed at the physically realistic values listed in Table 1.

3 RESULTS

3.1 VCSEL Reflectivity and Mode Structure

The normalized white-light reflectivity of the VCSEL (Figure 1b) reveals a high-reflectivity stopband extending from approximately 820 nm to 870 nm, consistent with the DBR design for an 845 nm laser. The laser mode appears as a narrow, shallow reflectivity minimum near 845 nm at the center of the stopband. On the short-wavelength shoulder of the stopband, two pronounced transmission dips are visible and are labelled dip A (≈ 793 nm) and dip B (≈ 810 nm). These dips correspond to leaky Fabry–Pérot resonances of the VCSEL cavity outside the high-reflectivity band and represent the only spectral windows at which optical spin injection can be efficiently coupled into the device without direct injection into the lasing mode.

Under electrical pumping alone, the VCSEL emits in two linearly polarized, orthogonally oriented fundamental modes separated in frequency by approximately 10 GHz (Figure 2a). This polarization splitting arises from the intrinsic birefringence of the VCSEL structure—a consequence of slight anisotropies in the gain medium and cavity—and is a characteristic feature of commercial VCSELs that must be accounted for in the SFM description through the birefringence parameter γ_p.

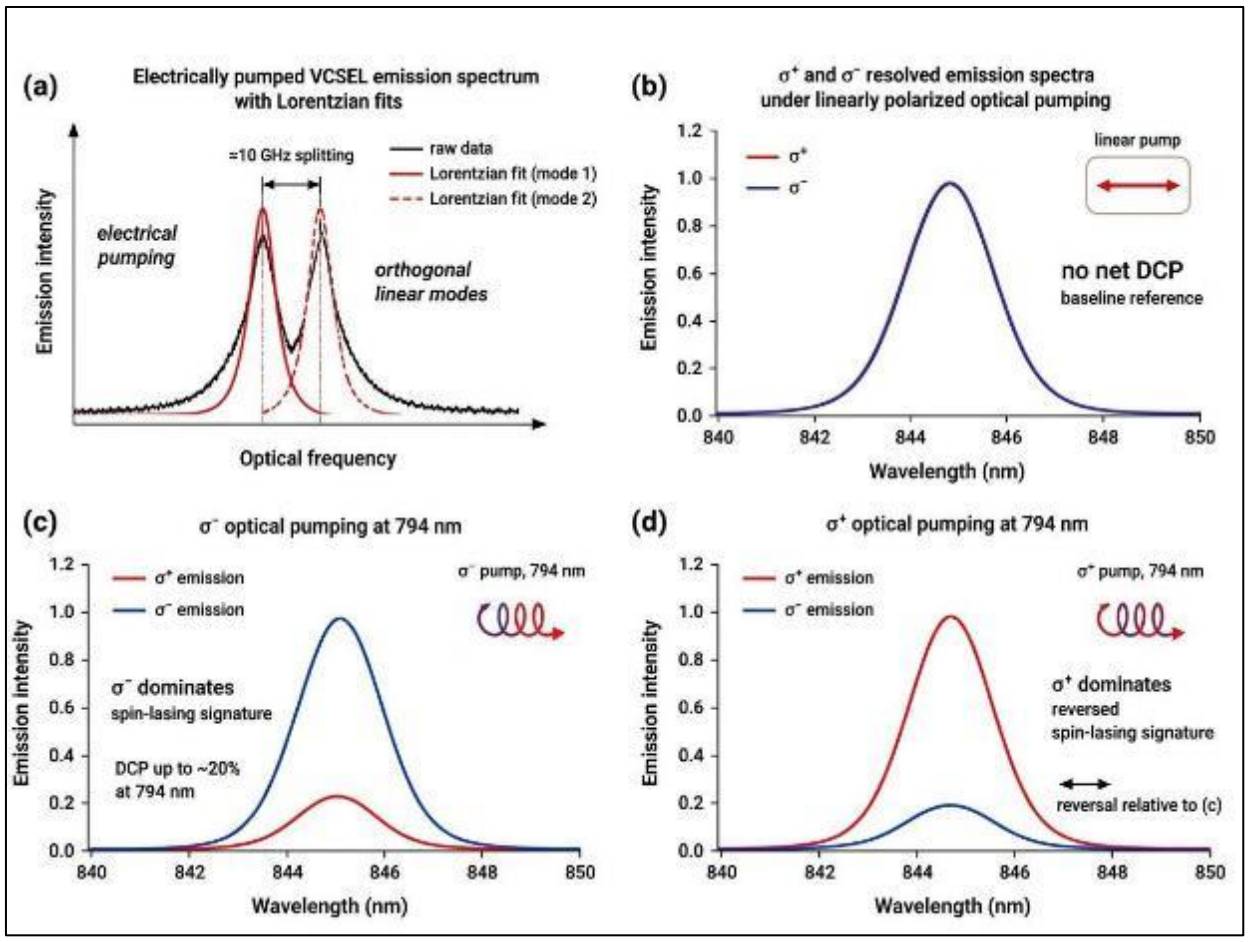


Figure 2: Polarisation-resolved VCSEL spectra and spin-lasing signatures. (a) Electrically pumped VCSEL spectrum with Lorentzian fits showing two birefringence-split orthogonal modes. (b) σ^+- and σ^--resolved spectra under linearly polarised optical pumping, providing the zero-DCP reference. (c) Circularly resolved emission under σ^- pumping at 794 nm. (d) Reversal of the dominant emission component under σ^+ pumping at 794 nm.

3.2 Spin Lasing at 794 nm (Dip A)

Under σ^- circularly polarized optical pumping at 793.3 nm (dip A), the VCSEL emission measured in the σ^- basis (Figure 2c) significantly exceeds that measured in the σ^+ basis for pump powers above the lasing threshold (Figure 3a, upper panel). This asymmetry—the canonical signature of spin lasing—is absent under linearly polarized pumping at the same wavelength and power (Figure 2b), while the corresponding reversal under σ^+ pumping is shown in Figure 2d,

confirming that the circular polarization of the emission originates from the spin-polarized carrier injection rather than any artifact of the optical path.

The DCP S_3 is plotted as a function of optical pump power in Figure 3a (lower panel). Below the threshold, S_3 remains near zero, consistent with the absence of coherent stimulated emission. Above the threshold, S_3 increases monotonically with pump power and saturates at approximately 20% at the highest accessible pump power. The saturation of DCP with increasing pump power is a well-understood feature of the SFM: as $\eta \to \infty$, the emission ellipticity ε asymptotes to the pump polarization P, as can be seen directly from equation (7).

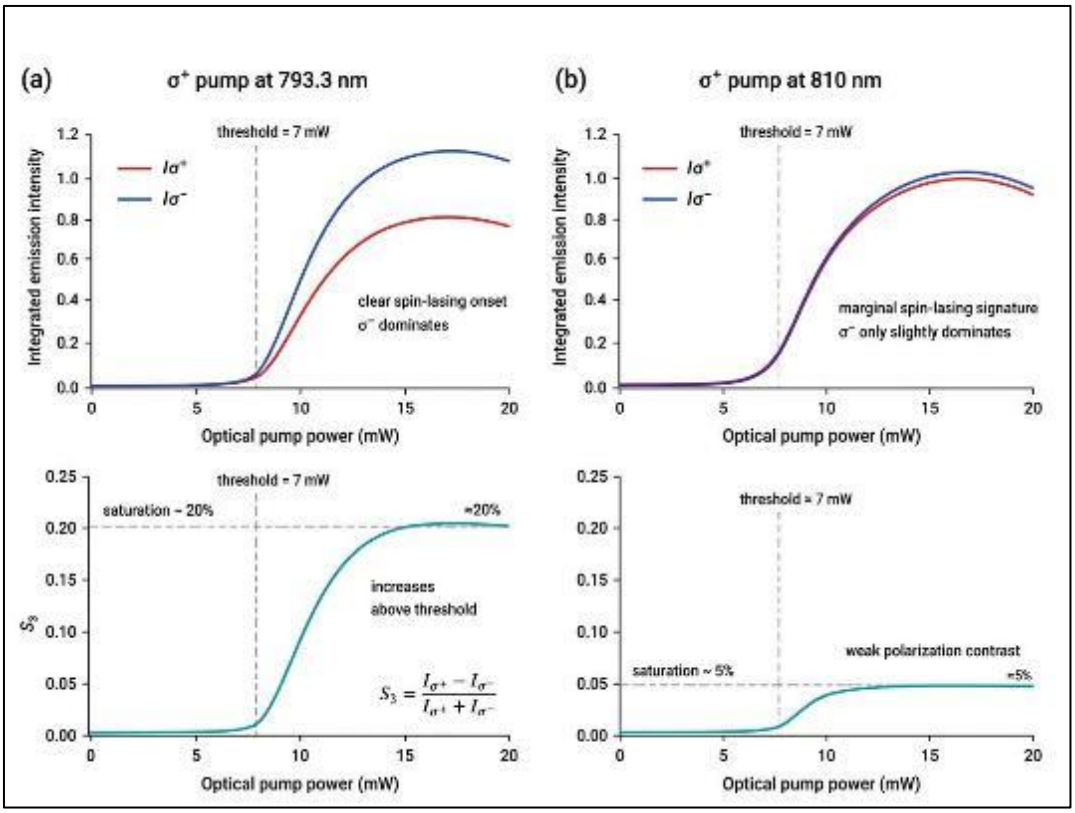


Figure 3: Light-in-light-out characteristics and circular polarisation versus pump power. (a) Integrated σ^+ and σ^- emission intensities and the corresponding third Stokes parameter S_3 under pumping at 793.3 nm. (b) Corresponding measurements under pumping at 810 nm. The dashed vertical lines mark the approximately 7 mW lasing threshold.

3.3 Spin Lasing at 810 nm (Dip B)

When the pump wavelength was tuned to 810 nm (dip B) with the same σ^- circular polarization, spin lasing was again observed, but with substantially reduced efficiency. The σ^- emission component was only marginally larger than the σ^+ component (Figure 3b, upper panel), and the DCP saturated at approximately 5% (Figure 3b, lower panel), a factor of four lower than at 794 nm. The symmetric reversal of the DCP sign under σ^+ pumping at both wavelengths confirms that the behavior is spin-dependent and not an artifact of optical misalignment.

The marked difference in maximum DCP between dips A (20%) and B (5%), despite identical device conditions and pumping protocol, is the central experimental finding of this work. Because the device temperature, current, and optical alignment were identical between the two measurements, the difference cannot be attributed to thermal or geometric factors. We identified the origin of the GaAs optical selection rules at finite crystal momentum, as discussed in Section 4.

3.4 Extended SFM Modelling

We applied equation (7) in Section 2.5 to reproduce the measured DCP versus pump power curves at both wavelengths. The model uses the parameter set listed in Table 1, with P as the only wavelength-dependent free parameter. Figure 4 shows the model predictions for the VCSEL emission ellipticity ε as a function of normalized pump power η under different assumed values of P.

Figures 4b–d illustrate the model ellipticity behavior at low, intermediate, and high pump powers, respectively. At low pump powers near threshold, ε is small and relatively insensitive to P. With increasing η, the ellipticity grows and eventually asymptotes to P, as demonstrated clearly on the logarithmic power axis in Figure 4d. This asymptotic behavior provides a direct read-out of the effective pump polarization from the high-power saturation value of the DCP, enabling a clean experimental determination of P.

By fitting the saturation values of 20% and 5% observed experimentally, the model yields best-fit values of P ≈ 0.20 for dip A (794 nm) and P ≈ 0.05 for dip B (810 nm). The model captures both the below-threshold suppression of DCP and the above-threshold rise and saturation, confirming that the extended SFM with wavelength-dependent P is sufficient to describe the experimental observations without invoking additional model parameters.

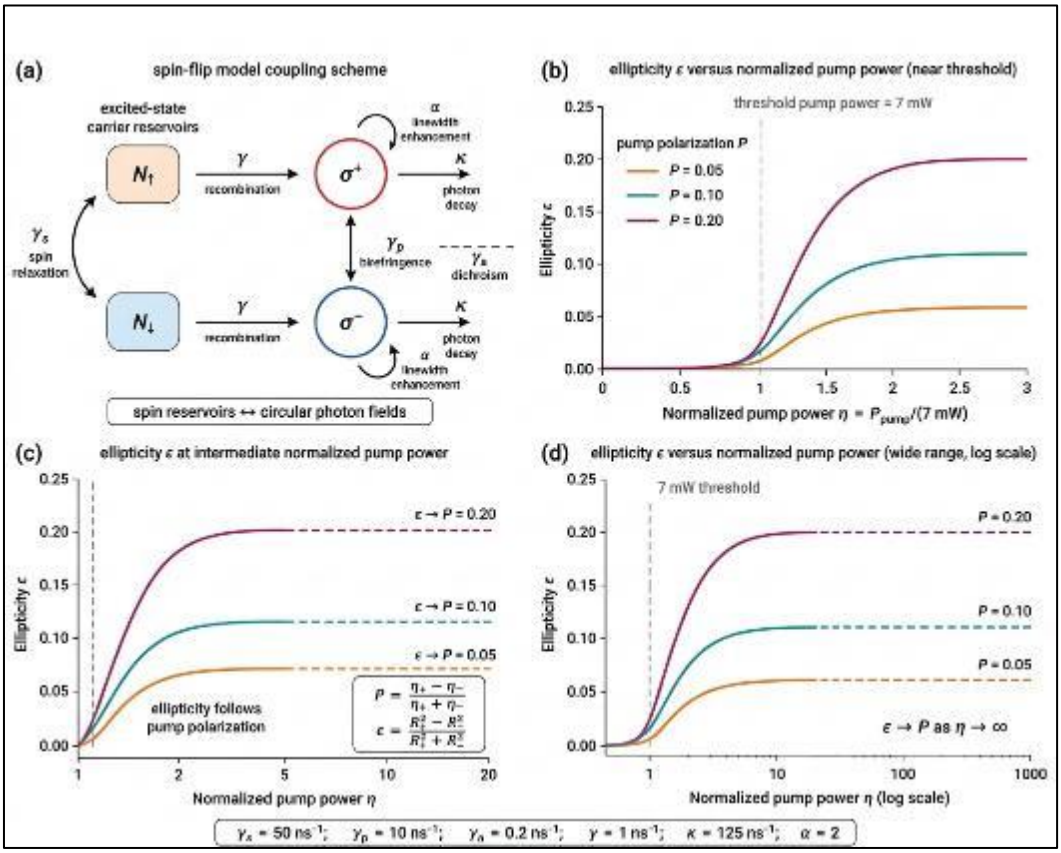


Figure 4: Spin-flip model coupling scheme and ellipticity versus normalised pump power. (a) Coupling between the spin-resolved carrier reservoirs and circular photon fields. (b) Modelled ellipticity near threshold for three pump-polarisation values. (c) Evolution of ellipticity at intermediate pump powers. (d) Wide-range logarithmic representation showing convergence of emission ellipticity to pump polarisation at high pump power.

4 DISCUSSION

4.1 Selection-Rule Origin of Wavelength-Dependent Spin Injection

The factor-of-four difference in saturation DCP between excitation at 794 nm and 810 nm requires explanation in terms of the microscopic physics of spin injection in GaAs. A naive argument based solely on energy relaxation would predict the opposite trend: excitation at 810 nm (closer to the 845 nm laser mode) involves less energy relaxation from the pump to the lasing state, which might be expected to reduce spin relaxation during carrier thermalization and thereby increase the injected spin polarization. The experimental observation that 794 nm excitation produces higher DCP therefore cannot be explained by spin relaxation during thermalization alone.

The resolution lies in the optical selection rules illustrated schematically in Figures 1c and 1d at finite crystal momentum ($k \neq 0$) in GaAs. At the Γ point ($k = 0$), excitation with σ^- circularly polarized light couples to both the heavy-hole (HH) and light-hole (LH) valence sub-bands with relative transition matrix elements of 3:1, respectively, leading to a maximum spin polarization of 50% in bulk GaAs [9, 19]. As the excitation energy increases above the HH band edge, the accessible k-vectors increase, and the LH band disperses upward in energy faster than the HH band because of its lighter

effective mass. As k increases toward the values corresponding to dip A (794 nm) excitation, the HH–LH energy splitting grows, reducing the LH contribution to the absorption. This effectively enhances the relative weight of the HH transitions, increasing the net spin polarization of the photo-excited carriers.

This picture is consistent with previous spectroscopic measurements of GaAs bulk and quantum-well systems. In bulk GaAs, the degree of optical polarization at the band edge is reported to be approximately constant up to 330 meV above the band edge [19, 24, 25], although subtle k-dependent corrections exist. In quantum-well structures, polarisation-resolved photoluminescence studies have demonstrated that excitation far from the E_0–HH transition (approximately 100 meV above at low temperature) produces approximately 50% co-polarized emission, whereas tuning toward the band edge reduces polarization due to enhanced coupling to the LH band [10, 11]. In our experiments, dip B (810 nm) lies closer to the HH band edge and therefore suffers greater LH admixture, leading to a lower effective P and reduced DCP. This is consistent with a recent study of spin polarization in quantum-dot vertical gain structures, which demonstrated that pump wavelength selection is a practical handle for optimizing spin injection independently of device geometry [21].

4.2 Implications for Device Optimisation

The present results have direct practical consequences for the design and operation of spin VCSEL systems. The DCP of approximately 20% achieved at room temperature with commercial, unmodified VCSELs is sufficient to deterministically bias the Stokes vector of the VCSEL output and trigger polarization switching in the bistable regime. This level of circular polarization has been identified as a threshold for reliable all-optical logic operations and for seeding neuromorphic photonic networks based on excitable spin-VCSEL nodes [15, 16, 26].

The key design principle emerging from our work is that, for VCSELs based on GaAs gain media, the optimal spin injection port among the available reflectivity dips is generally the one at the shortest accessible wavelength (highest energy), because this maximizes the HH contribution to the photo-excited spin polarization. This recommendation can be implemented without any modification to the VCSEL structure itself—it requires only an appropriate choice of pump laser wavelength, making it immediately applicable to existing commercial platforms.

The extended SFM developed here provides a quantitative predictive tool for evaluating the expected DCP for any combination of VCSEL parameters and pump wavelengths, given an estimate of P from the known selection rules at the targeted k-vector. Future work could refine the mapping from excitation wavelength to effective P by incorporating explicit k·p band structure calculations for the specific VCSEL material system or by empirically calibrating P across a wider range of pump wavelengths and temperatures.

4.3 Pathways to Higher DCP

Achieving a DCP significantly above 20% at room temperature in bulk GaAs VCSELs is fundamentally limited by the 3:1 HH:LH matrix element ratio at $k \approx 0$ and by the fast spin relaxation characteristic of room-temperature bulk GaAs ($\gamma_s \approx 50\ ns^{-1}$). Two principal routes to higher DCP can be identified from the present framework. First, replacing the bulk GaAs active region with a strained quantum-well or quantum-dot structure lifts the HH–LH degeneracy at $k = 0$ [20, 21], enabling 100% spin polarization of photo-excited carriers and substantially higher DCP in the VCSEL output. Second, operation at reduced temperature suppresses phonon-mediated spin relaxation, increasing the spin lifetime and the fraction of spin polarization preserved to the lasing threshold. Near-threshold DCP enhancement has been demonstrated in GaInNAs spin VCSELs at cryogenic temperatures [15], and the transition to room-temperature operation using optimized quantum-well designs has been identified as an important near-term target.

5 CONCLUSION

We demonstrated room-temperature spin injection into a commercial 845 nm VCSEL using non-resonant circularly polarized optical pumping at two wavelengths—794 nm (cavity dip A) and 810 nm (cavity dip B). Maximum degrees of circular polarization of approximately 20% and 5% were achieved at dips A and B, respectively. The factor-of-four difference in spin injection efficiency can be explained by the optical selection rules of GaAs at finite crystal momentum: excitation at 794 nm preferentially addresses the heavy-hole valence band, yielding a higher effective pump polarization, whereas excitation at 810 nm admits greater light-hole admixture, reducing the net spin injection.

To model these observations, we extended the well-known spin-flip model by introducing a wavelength-dependent effective pump polarization parameter P, while keeping all intrinsic VCSEL parameters fixed at physically realistic values. The extended model accurately reproduces the measured power-dependent DCP curves at both wavelengths, providing validation of the physical interpretation and a practical predictive framework for optimizing spin injection in commercial VCSEL platforms.

The 20% steady-state DCP demonstrated here is sufficient to bias the VCSEL Stokes vector deterministically and trigger polarization switching in off-the-shelf devices, directly enabling building blocks for all-optical logic, neuromorphic photonics, and spin-based communications without epitaxial or cavity redesign. Our results provide a clear design principle for wavelength-based optimization of spin injection in commercial GaAs VCSELs and establish a quantitative modelling framework applicable to a broad range of VCSEL material systems.

STATEMENTS ON COMPLIANCE WITH ETHICAL STANDARDS

Disclosure of conflict of interest

The author declares that he has no affiliations with or involvement in any organization or entity with any financial interest in the subject matter or materials discussed in this manuscript.

REFERENCES

[1] Žutić I, Xu G, Lindemann M, Faria Junior P E, Lee J, Labinac V, Stojšić K, Sipahi G M, Hofmann M R and Gerhardt N C 2020 Spin-lasers: spintronics beyond magnetoresistance Solid State Commun. 316–317 113949 https://doi.org/10.1016/j.ssc.2020.113949

[2] Drong M, Fördös T, Jaffrès H Y, Peřina J, Postava K, Pištora J and Drouhin H-J 2020 Local and mean-field approaches for modeling semiconductor spin-lasers J. Opt. 22 055001 https://doi.org/10.1088/2040-8986/ab7d8a

[3] Lindemann M, Xu G, Pusch T, Michalzik R, Hofmann M R, Žutić I and Gerhardt N C 2019 Ultrafast spin-lasers Nature 568 212–215 https://doi.org/10.1038/s41586-019-1073-y

[4] Yokota N, Nisaka K, Yasaka H and Ikeda K 2018 Spin polarization modulation for high-speed vertical-cavity surface-emitting lasers Appl. Phys. Lett. 113 171102 https://doi.org/10.1063/1.5040914

[5] Yokota N, Ikeda K and Yasaka H 2021 Spin-VCSELs for analog radio-over-fiber systems in 5G and beyond Proc. SPIE 11805 1180512 https://doi.org/10.1117/12.2593865

[6] Yang Y, Zhou P, Mu P and Li N 2022 Time-delayed reservoir computing based on an optically pumped spin VCSEL for high-speed processing Nonlinear Dyn. 107 2619–2632 https://doi.org/10.1007/s11071-021-07140-5

[7] Yigong Y, Huang Y, Zhou P and Li N 2025 Photonic reservoir computing for parallel task processing based on a feedback-free spin-polarized VCSEL Opt. Commun. 574 131225 https://doi.org/10.1016/j.optcom.2024.131225

[8] Mei-Ling Z, Jia X-H, Song W-J, Deng S-S, Bao M-Y, Tang Y-Q, Lv J-T, Li X-Y and Zhang X 2024 Jpn. J. Appl. Phys. 63 092004 https://doi.org/10.35848/1347-4065/ad7791

[9] Dyakonov M I (ed) 2008 Spin Physics in Semiconductors (Springer Series in Solid-State Sciences vol 157) (Berlin: Springer) https://doi.org/10.1007/978-3-540-78820-1

[10] Ivchenko E L and Pikus G E 1997 Superlattices and Other Heterostructures: Symmetry and Optical Phenomena 2nd edn vol 110 (Berlin: Springer) https://doi.org/10.1007/978-3-642-60650-2

[11] Pfalz S, Winkler R, Nowitzky T, Reuter D, Wieck A D, Hägele D and Oestreich M 2005 Optical orientation of electron spins in GaAs quantum wells Phys. Rev. B 71 165305 https://doi.org/10.1103/PhysRevB.71.165305

[12] Pan G, Xun M, Zhou X, Sun Y, Dong Y and Wu D 2024 Harnessing the capabilities of VCSELs: unlocking the potential for advanced integrated photonic devices and systems Light Sci. Appl. 13 229 https://doi.org/10.1038/s41377-024-01561-8

[13] Shitrit N 2024 Surface-emitting lasers meet metasurfaces Light Sci. Appl. 13 37 https://doi.org/10.1038/s41377-023-01369-y

[14] Huang Y, Zhou P, Torre M S, Li N, Henning I D and Adams M J 2021 Optically pumped spin-VCSELs: toward high-frequency polarization oscillations and modulation IEEE J. Quantum Electron. 57 1–12 https://doi.org/10.1109/JQE.2021.3111399

[15] Cemlyn B, Adams M, Harbord E, Li N, Henning I, Oulton R, Korpijärvi V-M and Guina M 2018 Near-threshold high spin amplification in a 1300 nm GaInNAs spin laser Semicond. Sci. Technol. 33 094005 https://doi.org/10.1088/1361-6641/aad42e

[16] Cemlyn B R, Henning I D, Adams M J, Harbord E, Oulton R, Korpijärvi V-M and Guina M 2019 Polarization responses of a solitary and optically injected vertical cavity spin laser IEEE J. Quantum Electron. 55 1–9 https://doi.org/10.1109/JQE.2019.2940041

[17] Adams M, Li N, Cemlyn B, Susanto H and Henning I D 2018 Algebraic expressions for the polarisation response of spin-VCSELs Semicond. Sci. Technol. 33 064002 https://doi.org/10.1088/1361-6641/aabda3

[18] HFE4192-581 datasheet: 4.25 Gbps 850 nm VCSEL LC TOSA (Finisar/II-VI)

[19] Meier F and Zakharchenya B P (eds) 1984 Optical Orientation (Modern Problems in Condensed Matter Sciences vol 8) (Amsterdam: North-Holland)

[20] Itskos G, Harbord E, Clowes S K, Clarke E, Cohen L F, Murray R, Van Dorpe P and Van Roy W 2006 Oblique Hanle measurements of InAs/GaAs quantum dot spin-light emitting diodes Appl. Phys. Lett. 88 022113 https://doi.org/10.1063/1.2163074

[21] Alhosiny N, Alharthi S S, Doogan J, Clarke E and Ackemann T 2025 Optimizing spin polarization in quantum dot vertical-gain structures through pump wavelength selection Appl. Phys. Lett. 126 191102 https://doi.org/10.1063/5.0261768

[22] Paschotta R 2024 Linewidth Enhancement Factor in the RP Photonics Encyclopedia https://doi.org/10.61835/2c8

[23] Al-Seyab R K, Adams M J and Henning I D 2015 Dynamics and polarization of conventional and spin-VCSELs in the presence of an axial magnetic field J. Opt. Soc. Am. B 32 683–691 https://doi.org/10.1364/JOSAB.32.000683

[24] Zakharchenya B P, Mirlin D N, Perel' V I and Reshina I I 1971 Spectrum and polarization of hot electron photoluminescence in semiconductors JETP Lett. 13 251

[25] Ekimov A I and Safarov V I 1970 Optical orientation of carriers in interband transitions in semiconductors JETP Lett. 13 177

[26] Harkhoe K, Verschaffelt G and Van der Sande G 2021 Neuro-inspired computing with spin-VCSELs Appl. Sci. 11 4232 https://doi.org/10.3390/app11094232

[27] Yokota N and Yasaka H 2021 Spin laser local oscillators for homodyne detection in coherent optical communications Micromachines 12 573 https://doi.org/10.3390/mi12050573